Laser processing of minerals common on asteroids

Anthony, Niklas

2021-03

Anthony , N , Frostevarg , J , Suhonen , H , Wanhainen , C , Penttila , A & Granvik , M 2021 , ' Laser processing of minerals common on asteroids ' , Optics & Laser Technology , vol. 135 , 106724 . https://doi.org/10.1016/j.optlastec.2020.106724

http://hdl.handle.net/10138/324275
https://doi.org/10.1016/j.optlastec.2020.106724

Optics & Laser Technology 135 (2021) 106724

Contents lists available at ScienceDirect

Optics and Laser Technology

journal homepage: www.elsevier.com/locate/optlastec

Full length article

Laser processing of minerals common on asteroids

Niklas Anthony [a,*], Jan Frostevarg [b], Heikki Suhonen [c], Christina Wanhainen [d], Antti Penttilä [c], Mikael Granvik [a,c]

[a] Asteroid Engineering Lab, Onboard Space Systems, Luleå University of Technology, Box 848, 98128 Kiruna, Sweden
[b] Department of Engineering Sciences and Mathematics, Luleå University of Technology, 97187 Luleå, Sweden
[c] Department of Physics, P.O. Box 64, 00014 University of Helsinki, Finland
[d] Department of Civil, Environmental and Natural Resources Engineering, Luleå University of Technology, 97187 Luleå, Sweden

ARTICLE INFO

Keywords:
Laser drilling
High-speed imaging
X-ray micro-tomography
Asteroid mining

ABSTRACT

Asteroid mining and redirection are two trends that both can utilize lasers, one to drill and cut, the other to ablate and move. Yet little is known about what happens when a laser is used to process the types of materials we typically expect to find on most asteroids. To shed light on laser processing of asteroid material, we used a 300-W, pulsed Ytterbium fiber laser on samples of olivine, pyroxene, and serpentine, and studied the process with a high-speed camera and illumination laser at 10 000 frames per second. We also measure the sizes of the resulting holes using X-ray micro-tomography to find the pulse parameters which remove the largest amount of material using the least amount of energy. We find that at these power densities, all three minerals will melt and chaotically throw off spatter. Short, low-power pulses can efficiently produce thin, deep holes, and long, high-power pulses are more energy efficient at removing the most amount of material.

1. Introduction

Asteroid mining has the potential to be a very profitable industry [1]. Sourcing nickel–iron family metals from asteroids has gained interest since 1977 [2], and it was shown to be as economically competitive as extracting the metals from the Moon [3]. Volatiles like water can be extracted from asteroids and used as rocket fuel [4] and even raw, unprocessed material can be used as radiation shielding [5]. The only feasible way to thoroughly prospect an asteroid is to study it with a robotic spacecraft, capable of getting below the surface. Although remote analysis methods like X-ray spectroscopy have been space-proven by the Dawn mission [6], their findings have some ambiguity that should be resolved by in-situ verification.

Using a drill or shovel would require landing on a small body, which presents several challenges such as the lack of knowledge of surface strength (i.e., powdery or stoney) and accounting for rotation or even tumbling. A summary of some landing/anchoring and sampling technologies with advantages and disadvantages is given in [7]. One solution to these challenges would be to use a laser to drill beneath the surface. Because there are no moving parts, it produces negligible counter-torques, and will not get stuck. It also has the advantage of being able to function on a diverse range of targets, from dust to solid metal; see Section 8 of [8] for publications related to various materials. They could even be used without having to land: a diffraction-limited Nd:YAG laser (wavelength 1070 nm) with a 34-cm aperture can make a 1-mm spot at a distance of 1 km.

The first laser was built in 1960 [9], and the first patent on laser drilling was filed in 1964 [10]. The first mathematical model of the drilling process was developed in 1976, which studied hole size and drilling rate on a copper plate [11]. Since then, High-Speed Imaging (HSI) has been useful in understanding the processes occurring when drilling, piercing, and cutting metals, such as spatter [12], melt dynamics, [13] and the gas effect [14], to name a few. By properly tuning the laser repetition rate and pulse width, the drilling efficiency has been shown to improve by a factor of 27 [15]. Lasers have also been tested on natural materials such as shale and sandstone [16], granite [17], and slate [18]. These were mostly for industrial purposes like cutting or engraving, and did not study the process in detail. Lasers have been used to process bauxite and red mud in [19], gold ores in [20], and is also used as a sampling tool when studying trace element chemistry of sulfides by mass spectrometry [21].

The first laser intended for use in space was the LIMA-D instrument

Abbreviations: DE, Depth Efficiency; VE, Volume Efficiency; XMT, X-ray Micro-Tomography; fps, frames per second.

* Corresponding author.
E-mail address: niklas.anthony@ltu.se (N. Anthony).

https://doi.org/10.1016/j.optlastec.2020.106724
Received 22 April 2020; Received in revised form 12 October 2020; Accepted 29 October 2020
Available online 21 November 2020

Table 1
The main chemical and physical characteristics of test samples: olivine, pyroxene (clino-), and serpentine [28]. The letter M_1 can be Mg or Fe, M_2 can be Ca or Na, M_3 can be Mg, Fe, or Al, M_4 can be Mg, Fe, Ni, Mn, or Zn, and M_5 can be Si, Al, or Fe.

Mineral group	Chemical composition	Mohs hardness	Specific gravity
Olivine	$(M_1)_2SiO_4$	6.5–7.0	3.2–4.4
Pyroxene	$(M_2)(M_3)\ Si_2O_6$	5.0–6.5	3.2–3.6
Serpentine	$(M_4)_3(M_5)_2O_5(OH)_4$	3.0–6.0	2.5–2.6

on the Phobos 1 and 2 spacecraft launched in 1988 [22]. It was supposed to perform laser-ablated mass spectroscopy to determine the surface composition of the Martian moon, but unfortunately the mission was unable to reach this phase, and the instrument went unused. A laser is currently in use on the Mars, via the Curiosity rover, conducting Laser-Induced Breakdown Spectroscopy (LIBS) experiments on the natural materials on the Martian surface [23]. A similar process is also being suggested to determine asteroid composition using small satellites [24].

The majority of asteroids in the main belt and in the near-Earth region have spectral types S (~60%) or C (~20%), that stand for siliceous and carbonaceous, respectively [25]. Olivine and pyroxene are thought to be the dominant minerals for S and C types [26], and were therefore selected for the present study. Serpentine was also selected, because serpentine-group minerals are the most common hydrated minerals in meteorites [27]. Table 1 provides the main chemical and physical characteristics of the samples following [28]. The specific heat capacities for olivine, pyroxene, and serpentine are roughly 1.5, 1.1, and 1.3 kJ kg^{-1} K^{-1}, respectively. Iron-rich olivine (fayalite) begins to melt at 1763 K, while magnesium-rich olivine (forsterite) does not begin to melt until 2436 K [29]. In liquid form, gases like MgO, FeO, and SiO_2 begin to appear, so it is difficult to say at what temperature olivine begins to vaporize, if at all in its full mineral form [30]. As olivine is one of the first minerals to crystalize while cooling, we will assume the melting temperatures for our pyroxene and serpentine samples are below that of olivine.

Laser-induced ablation has also been suggested as a method of redirecting potentially dangerous asteroids since 1994 [31]. They simulated a solar concentrator by using a laser on a sample of basalt and studied the evaporation force using a pressure plate. Experiments with olivine were conducted to test the usefulness of a laser for asteroid redirection [32]. Force measurements on pyroxene as well as high-fidelity asteroid simulant powder were performed with sub-nanosecond pulses, also for the purpose of asteroid redirection [33].

The main purpose of our research is twofold: first, to understand how natural materials respond to laser irradiation, and second, to explore how varying laser pulse parameters affects the hole depth and the volume removed. We use millisecond pulses, which we believe is most suitable for a piercing experiment, whereas nano- to femto-second pulses mostly operate in a shallow ablation mode. By studying the process with HSI, we are able to see exactly what processes occur, be they melting, vaporization, explosion, etc, and how, exactly, the process differ from one mineral to the next. By studying the hole depths and volumes, the question how pulse parameters affect the depth and the volume removed can be answered.

2. Methodology

First, the three samples—olivine, pyroxene, and serpentine—were cut into roughly 1 cm thick slices to perform experiments on. A reflectance spectra was obtained of each sample, and in addition, thin sections of each rock were taken for petrographic analysis. During each experiment, HSI was applied at the laser beam-surface interaction point. Once the experiments were finished, the samples were further cut and analyzed with an X-ray Micro-Tomography (XMT) device. We describe the methodology in greater detail in the following subsections.

Table 2
Laser parameters.

Parameter	Value
Wavelength	1070 nm
Source power	< 300 W
Pulse frequency	< 500 Hz
Spot width	100 μm
Beam quality	8 mm mrad
Focal length	220 mm

2.1. Sample characterization

Reflectance spectra of the samples were measured over the visual and near-infrared wavelengths 450–1150 nm. The measurements were carried out using a Light Tec Reflet 180S goniometer in a measurement geometry with 8° incidence and 0° measurement angles. The spot size from the incident illumination on the sample was about 1 cm in diameter. The reflected signal was recorded with an Ocean Optics Maya2000 Pro spectrometer and the calibration of the measured signal was done using a LabSphere Spectralon diffuse reflectance standard. Two spots from each of the three samples were selected from the most prominent phase of the material. All the materials are measured with the same settings and calibrated against a diffuse reflectance standard, so their absolute reflectance levels can be compared.

Petrographic studies were carried out to characterize the test samples and to provide further compositional and textural information that could be relevant for the laser performance (impurities, cleavage planes, etc). The polished thin sections were prepared by Precision Petrographics Ltd (Canada) and were studied in an optical microscope (Nikon ECLIPSE E600 POL) using cross-polarized light.

The XMT measurements to characterize the resulting holes were carried out with a GE phoenix nanotom s system. The samples were imaged at 25 μm voxel size, with X-ray generator settings at 100 kV and 150 μA, using a 0.5 mm Cu filter. A total of 1000 projection images were recorded over a 360° rotation of the sample (0.36° step) with 1.5 s exposure time for each projection. The 3D volume data was reconstructed from these data sets using datos—x reconstruction software version 2.4.0.1199 (GE phoenix).

The 3D volumetric data was analysed using the free software Fiji (ImageJ) by first manually choosing and labeling the locations of the holes in the 3D volumes [34,35]. The grayscale voxel data (corresponding to "radiodensity" which is a function of density and the average atomic number) was then filtered with a 3D median filter and thresholded using a value selected to be $I_{th} = I_{bg} + 0.7\cdot(I_{mat} - I_{bg})$, where I_{bg} and I_{mat} are the average grayscale values in the background (surrounding air) and the matrix of the sample (excluding metal impurities), respectively. Binary image operations to clean and join isolated objects were then applied before the volumes and lengths of each hole were printed to a file for further analysis. The uncertainties for the measurements for both volume and depth were less than 2%.

2.2. Laser experiment and observation

The experiments were conducted with a YLR-300-MM-AC Ytterbium fiber laser, in an autonomous mode, from IPG Photonics, with capabilities given in Table 2. The laser head was mounted in a fume hood and connected via fiber-optic cable to the source located outside the hood. To better simulate the effects of zero gravity, the experiment was conducted horizontally, to prevent molten material from pooling in the bottom of the hole. The laser head was angled 10° from horizontal to prevent reflected processing light and ablated material from damaging the optics. A shielding gas of Argon was placed near the surface of the targets to prevent oxidation of the experiment samples. The target was mounted to a moving platform (CNC machine) capable of re-positioning between experiments and controlling the focal distance. The surface of

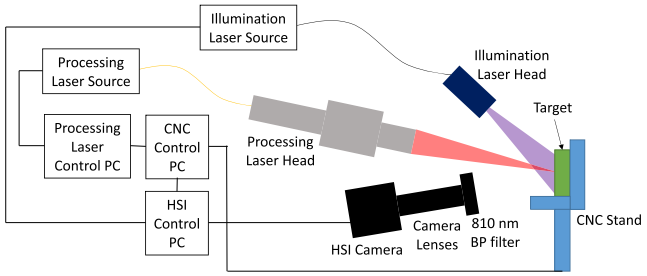

Fig. 1. Experiment setup.

			Pulse gap (ms)											
			1			2			3			4		
		Power (W)	100	200	300	100	200	300	100	200	300	100	200	300
Pulse length (ms)	Olivine	1												
		2												
		4												
		8												
		16												
	Pyroxene	1												
		2												
		4												
		8												
		16												
	Serpentine	1												
		2												
		4												
		8												
		16												

Fig. 2. Overview of which laser parameters (power, pulse length, and pulse gap) were used in the experiments. The grey boxes indicate an experiment was performed at the corresponding pulse parameters, and white boxes indicate no experiment was performed.

the samples were placed in the focal plane, which allowed for power densities up to 954.9 kW/cm^2.

The HSI system used in this experiment is based on the one used in [13]. A high-speed camera (FASTCAM Mini UX100 type 800-M-16G) running at 10 000 frames per second (fps) was used to study what physical processes happen during illumination. The light produced during processing over-saturated the CCD detector in the camera, thus a filter allowing only 810 nm light through was placed in front of the lens of the camera to reduce the processing light. An illumination laser of the same wavelength (810 nm) (CaviLux HF) was configured to illuminate the target area, which provided a clear view of the behavior of the material. The illumination laser was configured to have 10 µs pulses at 10 kHz, and the camera had an exposure time of 4 µs. An overview of the entire experiment setup is given in Fig. 1.

There were three independent variables in the experiments: laser power, pulse width, and repetition rate. The power was varied from 100 W to 300 W, the pulse widths from 1 ms to 16 ms, and the repetition rate from 53 Hz to 500 Hz. The repetition rate was selected to give integer values of pulse gaps from 1 ms to 4 ms. As it is assumed that olivine is the most abundant mineral of the three, it was selected for a wide range of experimental parameters. The pyroxene and serpentine had a narrower, and more specific range of parameters, based on iterative analysis of high-speed footage viewed while performing the experiments. We started with a regular matrix of parameters, but it turned out that many of the chosen parameters would not provide useful results. So we decided to use the pulse settings that seemed to produce the largest amount of spatter during the initial olivine experiments also on the other two samples. A summary of the pulse settings space is given in Fig. 2. In addition, several "continuous mode" experiments were run to observe long-term behavior, each lasting ~350 ms.

The pulse parameters were set using the software provided with the laser itself, and an on–off trigger signal was sent from the CNC controller PC. Pulse modulation is done via selective voltage control (power modulation). Before the on signal was sent, the CNC PC would also toggle the crossjet and shielding gases and send a trigger signal to the HSI PC. The HSI PC, running Photron FASTCAM Viewer software, would then activate the illumination laser and begin recording for approximately 1 s, which is longer than all the experiment durations. After the laser-off signal was sent by the CNC PC, the gases and lasers would be shut off. The HSI PC ws then used to clip and save the experiment from the 1-s recording.

An important note is that the number of pulses varied for each experiment due to the synchronization signals having delays. Some experiments were repeated multiple times in order to test how sensitive the results were to local variations in the material composition and structure. The samples were not uniform crystals so their compositions and structures varied across their surfaces, especially for pyroxene and serpentine.

3. Results

The results are grouped into three parts. The first part concerns the characterization of the samples, which include images to show the overall characteristics of the samples. It also includes the results of the spectral analysis and petrographic studies. The second part is about the HSI, showing the processes that occur on each sample at varying depths. The third part is a study of the size and shape of the holes, including processing efficiencies.

3.1. Sample pre-characterization

Imaging in visual wavelengths reveals the overall variation between and on the samples (Fig. A.1). The olivine sample shows evenly distributed dark and light lithologies, with what looks like metallic iron or iron sulfide near the middle bottom. The pyroxene sample has an

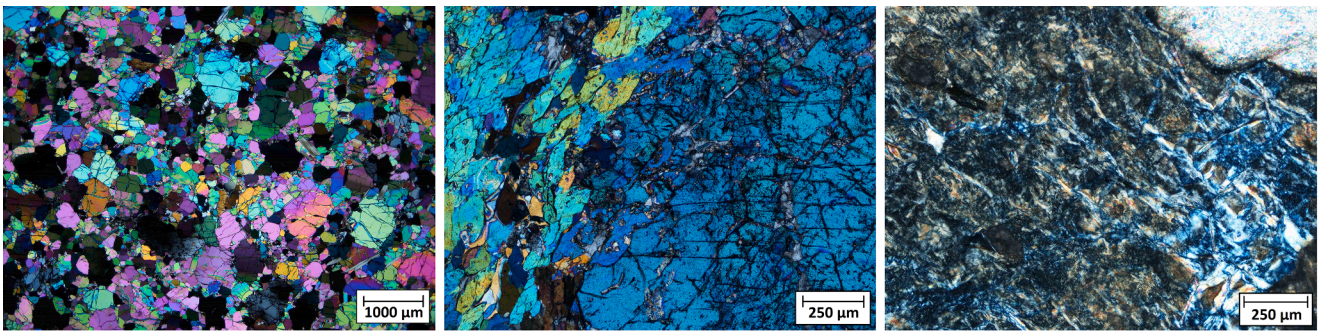

Fig. 3. Photomicrographs taken in cross-polarized light of olivine (left), pyroxene (middle) and serpentine (right) test samples.

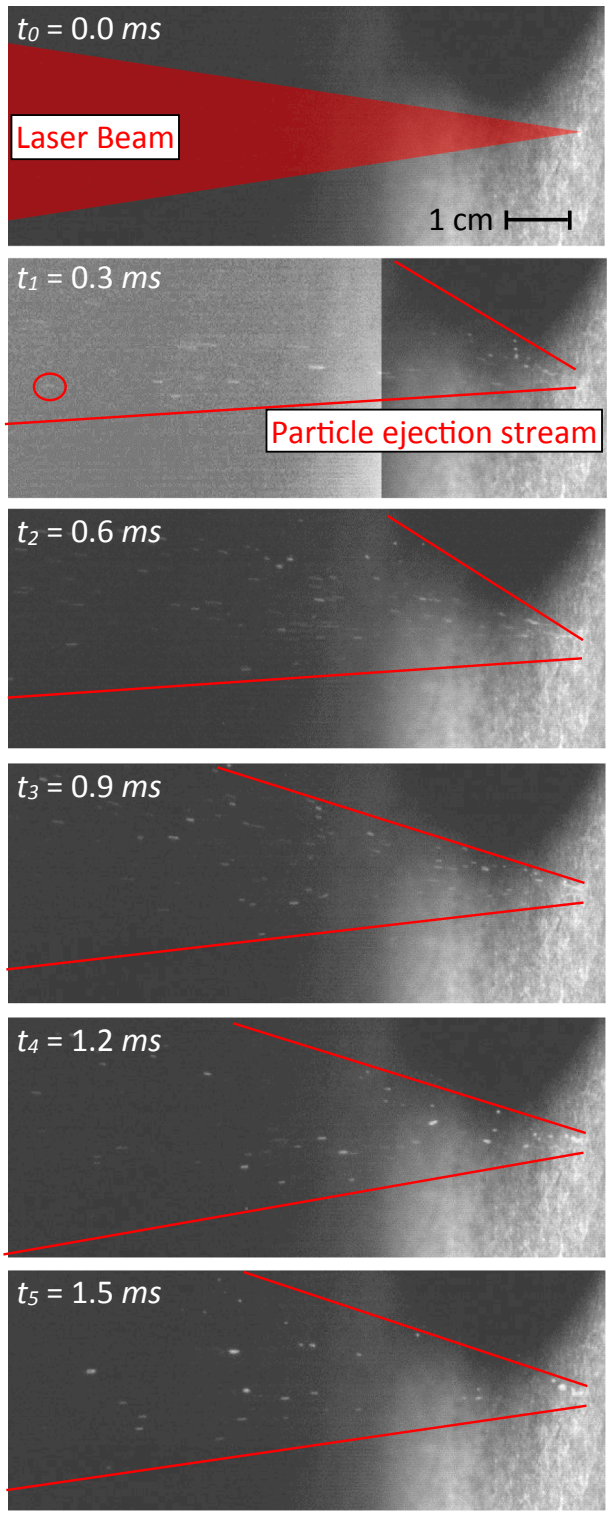

Fig. 4. High-speed footage of pyroxene during the initial moments of the first pulse. Laser power was 300 W with 4 ms on time and 1 ms off time. The left side of the second frame has been brightened to show the furthest discernible particle.

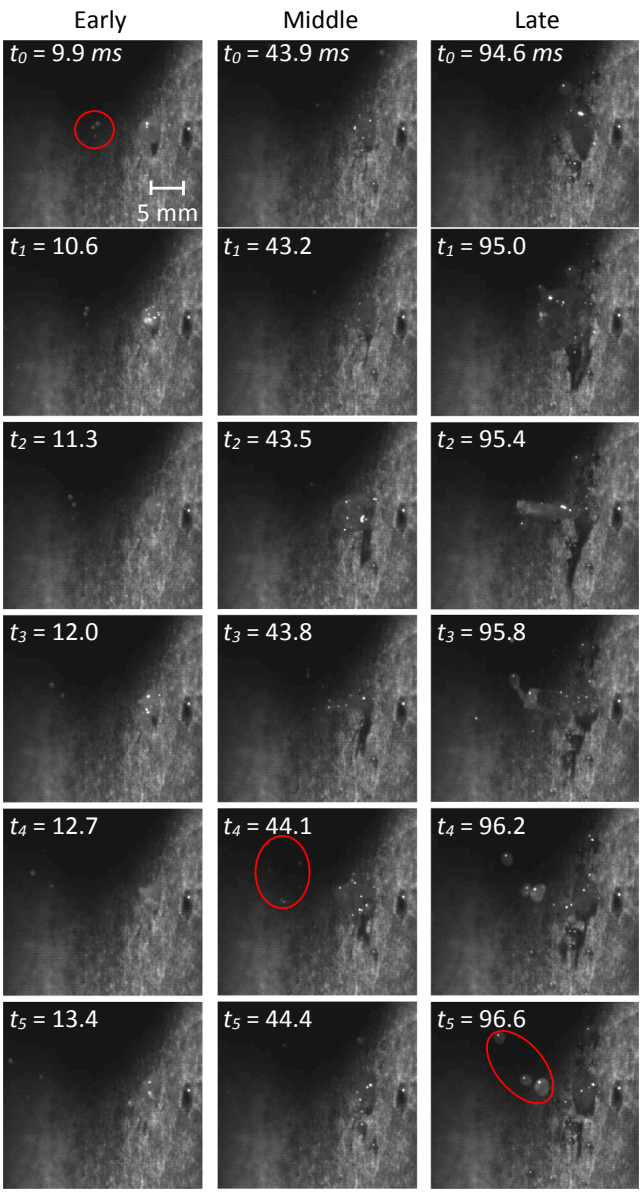

Fig. 5. Selected frames showing the behavior of pyroxene under laser irradiation over time. The pulse settings are 4 ms on and 1 ms off at 300 W. The frames in the near-surface, mid-depth, and deep series are 0.7, 0.3, and 0.4 ms apart, respectively. The red circles highlight the spatter for each series. (For interpretation of the references to colour in this figure legend, the reader is referred to the web version of this article.)

overall smooth grey/white/blue color, with some characteristic cleavages throughout the surface. The serpentine contains brown, yellow, and green regions, with spots and cracks all over the surface. There is a dark blue region in the bottom as well.

The reflectance spectra is shown in Fig. A.2. Both the olivine and pyroxene materials are showing the absorption band (pyroxene) or overlapping bands (olivine) around ~1000 nm. It can be noted, that the reflectance levels of the serpentine material are clearly higher compared to the olivine and pyroxene materials at the wavelength of the laser, at 1070 nm. With the assumption that all the three materials have quite similar, diffuse angular scattering profiles, we can argue that the higher reflectance of serpentine indicates also lower absorption in the material, which also indicates that a smaller fraction of incident power is available for material heating.

The petrographic analysis reveals the microstructure of segments of the samples (Fig. 3). The olivine thin section reveals olivine crystals with diagnostic cracks and third-order interference colors. The sample is slightly mica altered, meaning a small amount of the olivine converted to mica, and contains accessory iron sulfides and iron oxides. The pyroxene thin section contains pyroxene crystals with second-order interference colors and small parts altered to calcite. The left part of the pyroxene image shows the 87° cleavage intersection usually

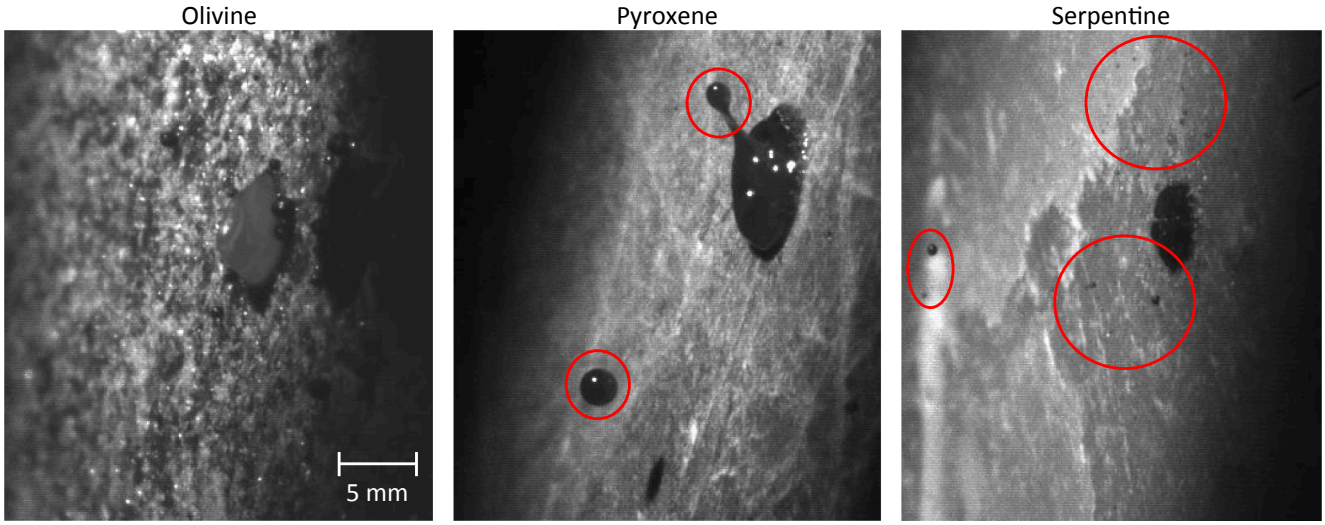

Fig. 6. Images from the continuous-mode experiments. From left to right are olivine, pyroxene, and serpentine. No ejection is visible from olivine, and red circles show large spatter from pyroxene, and fine spatter from serpentine. (For interpretation of the references to colour in this figure legend, the reader is referred to the web version of this article.)

associated with pyroxene. The serpentine thin section shows typical low first-order interference colors and mesh texture. Iron oxides/hydroxides are present in the sample as is a relict olivine crystal in the top right corner of the image.

3.2. High-speed imaging analysis

High-speed footage revealed a number of intriguing processes occurring during interaction of the processing laser beam and the minerals. The olivine and pyroxene samples rapidly ejected small (sub-millimeter-sized) particles in the initial moments of illumination (Fig. 4). At t_0, the laser begins irradiating the pyroxene surface. After 0.3 ms, particles have already reached the far left part of the image, a distance of roughly 7 cm. We estimate that these particles travel at over 230 m/s, the escape velocity of a 360-km-wide asteroid. The opening angle of the stream is ~25° and the rapid outburst lasts roughly 1.5 ms.

As the cavity depth increases and heat accumulates, the material begins to melt. The rapid ejection of material then stops, most likely due to the surface tension of the melt pool, and is replaced by a different process where molten material is cast off in larger chunks (over 1 mm in size) at slower speeds, ranging from 5 m/s to 30 m/s (5 m/s is the escape velocity of a 7.5-km-wide asteroid), and in all directions. This can be demonstrated with an experiment on pyroxene, where the power is 300 W, pulse width of 4 ms, and repetition rate of 200 Hz (Fig. 5). The figure is divided into three phases: early, middle and late. The "early" series starts at the third pulse, showing a relatively small melt area, 1–2 mm in width, and ejection of relatively small spatters, less than 1 mm in size. By the time the ninth pulse is over (the beginning of the "middle" phase), the melt pool has increased in size to 2–3 mm, and is ejecting more and larger spatter, up to 1 mm in diameter. The "late" series shows the 19th pulse, where the melt area is relatively large, roughly 4–5 mm, and the ejected spatter is also relatively large, 1–2 mm in size. The same overall behavior was observed for olivine and serpentine (Figs. A.3 and A.4, respectively), except that the initial outburst was not seen for serpentine.

An interesting phenomenon seen in olivine and pyroxene is a tendril-like formation, which extended roughly 1 cm from the melt pool before emitting a large (1–2-mm) particle at the tip, and then retracted back. An example of this phenomenon is seen at t_0 in the late series in Fig. A.3, and another less pronounced one at t_1 in the middle series.

The continuous-mode experiments showed similar behaviors to pulsed experiments (Fig. 6). In the olivine sample, a melt pool of material extending roughly 1 mm above the surface formed and slowly grew to 5 mm in diameter. It undulated vertically from the surface, but did not throw off much spatter. The pyroxene exhibited a similar bulge above the surface, but threw off large pieces (1–2 mm in diameter) of spatter frequently (roughly 1 per millisecond) throughout the experiment. One can also see evidence of the tendril like formation. The serpentine did not have a large melt pool extending above the surface, but threw off spatter of small (micrometer-sized) and medium (1-mm-

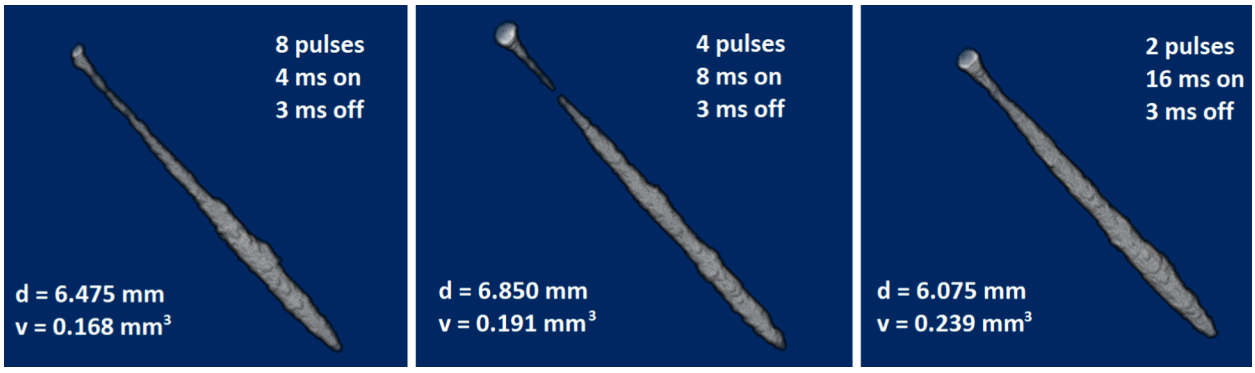

Fig. 7. XMT images of three holes in the olivine sample. Each hole was created by 9.6 J of energy at the 300-W power setting. Shown are the pulse parameters, number of pulses, d for depth, and v for volume removed.

Pulse Length (ms)		Pulse gap (ms) 1	2	3	4
Ol. 200 W	1	0.79		0.975	
	2	0.745	0.292	1.008	
	4	0.828	1.484	0.906	
	8	0.697		0.598	
	16	0.492		0.467	
Ol. 300 W	1	0.895		0.907	
	2	0.756	0.986	1.031	
	4	0.564		0.674	
	8	0.441		0.714	
	16	0.327		0.633	
Py. 300 W	1	1.049			
	2				0.994
	4	0.320		0.891	
	8				
	16	0.420		0.405	
Se. 300 W	1	0.563			
	2				
	4	0.451		0.559	
	8			0.466	
	16			0.413	

Fig. 8. Hole depth in mm per joule added for pulsed experiments. Color increases in intensity with an increase in depth. Blank cells indicate no experiment was performed with the corresponding pulse parameters. (For interpretation of the references to colour in this figure legend, the reader is referred to the web version of this article.)

sized) pieces nearly constantly throughout the entire experiment.

On all three samples, after the laser was switched off, the melt pools rapidly increased in size, forming semi-translucent bubbles and ejecting material, until it cooled completely (Fig. A.5), though the serpentine sample's bubbles were not as large.

3.3. Hole sizes and shapes

After the laser experiments, the samples were cut again to be better suited for the XMT studies. Each of the resulting XMT images is oriented that the surface of the sample is in the top left of each image, and drilling "down" is in the bottom-right direction. Due to the fact that the number of pulses varied between experiments and between samples, it is difficult to directly compare the shapes, structure, and sizes of the holes. There were, however, a few comparable situations. For instance, there is a clear increase in volume removed when increasing the pulse length while maintaining the power (300 W), gap between pulses (3 ms), and total energy (9.6 J) (Fig. 7).

Another interesting thing can be seen comparing the holes of the continuous-mode tests (Fig. A.6); the holes are roughly the same depth (11 mm), but the serpentine hole is nearly twice as wide near the bottom. The difference in shape could be due to the sheet-like structure of serpentine, which funneled energy sideways instead of downward. The pyroxene hole was larger than the others, possibly due to the cleavages breaking off, instead of a smooth melt.

Eleven out of 36 holes in the olivine sample had discontinuities close to the surface (Fig. A.7). There seems to be no correlation to laser power or pulse settings. The discontinuities could be caused when liquid from the bottom cools and solidifies before it exits the hole, sometimes even closing the hole.

Accurate numbers of laser pulses were derived by analyzing the high-speed video footage. The total energy that was injected into the rocks was calculated by multiplying the energy per pulse (multiply the laser power by the pulse duration) by the number of pulses. The volume and

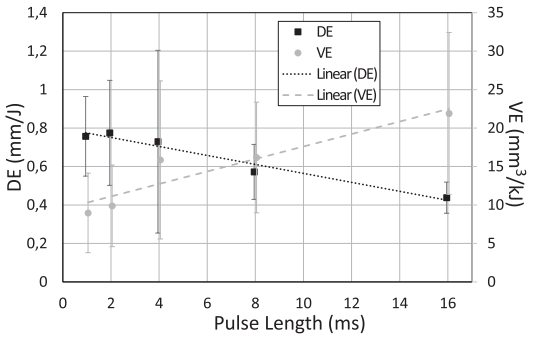

Fig. 9. Depth (DE) and volume (VE) processing efficiencies by pulse length.

Pulse Length (ms)		Pulse gap (ms) 1	2	3	4
Ol. 200 W	1	5.400		5.500	
	2	9.327	2.083	5.000	
	4	8.281	17.188	8.750	
	8	9.375		10.651	
	16	7.891		9.609	
Ol. 300 W	1	13.684		4.912	
	2	19.359	11.667	15.208	
	4	16.154		17.500	
	8	25.243		19.896	
	16	24.000		24.896	
Py. 300 W	1	17.222			
	2				11.190
	4	31.081		17.917	
	8				
	16	28.472		36.736	
Se. 300 W	1	15.667			
	2				
	4	21.771		20.139	
	8			23.229	
	16			17.465	

Fig. 10. Volume removed in mm^3 per kilojoule added for pulsed experiments. Color increases in intensity with an increase in volume removed. Blank cells indicate no experiment was performed with the corresponding pulse parameters. (For interpretation of the references to colour in this figure legend, the reader is referred to the web version of this article.)

depth for each hole is divided by the total energy of the experiment to find volume efficiency (VE) and depth efficiency (DE), respectively. These values can then be compared to the corresponding pulse parameters. The values for the experiments that were run more than once are the averages. The measurement values for groups of data (i.e. all olivine experiments) are the averages and the standard deviations.

The DE results suggest that olivine is the easiest to process, having an average DE of 0.722 ± 0.336 mm/J, and serpentine the most difficult, averaging 0.492 ± 0.080 mm/J, with pyroxene in between with an average DE of 0.589 ± 0.286 mm/J (Fig. 8). In general, our results suggest the shorter the pulse is, the more energy efficient the depth processing is, see the dotted line in Fig. 9. Allowing a longer gap, that is, reducing the repetition rate, also seems to increase the efficiency. For experiments with a 1-ms gap, the average DE was 0.586 ± 0.205 mm/J, while those with a 3-ms gap had an average of 0.663 ± 0.291 mm/J. The averages of the 200-W and 300-W experiments were 0.735 ± 0.327 mm/J and 0.713 ± 0.234 mm/J, respectively.

The VE results seem to paint a different picture, suggesting that pyroxene is the easiest to process, having an average VE of 22.3 ± 13.0

Table 3
Processing efficiencies for the pulsed experiments with a laser power of 100 W. VE stands for volume efficiency and DE stands for depth efficiency.

Material	Pulse width (ms)	Pulse gap (ms)	VE (mm^3/kJ)	DE (mm/J)
Olivine	2	2	5.833	0.417
Olivine	4	2	5.625	1.063
Olivine	4	4	5.000	0.359
Pyroxene	1	1	4.211	0.434
Serpentine	1	1	2.857	0.554

Table 4
Processing efficiencies for continuous-mode experiments. VE stands for volume efficiency and DE stands for depth efficiency.

Material	Power (W)	Duration (ms)	VE (mm^3/kJ)	DE (mm/J)
Olivine	200	376	8.684	0.127
Olivine	300	313	19.375	0.121
Pyroxene	300	380	23.219	0.098
Serpentine	300	380	19.404	0.098

mm^3/kJ, and olivine is the most difficult, with an average VE of 11.9 ± 6.8 mm^3/kJ; serpentine was in the middle with an average 16.2 ± 6.7 mm^3/kJ (Fig. 10). The difference in VE could be due to the cleavages associated with pyroxene, where chunks of the mineral could be broken off from the sides of the processing hole. It appears that the longer the pulse, the more efficiently the material is removed, see the dashed line in Fig. 9. Pulses with 1-ms gaps had an average VE of 16.8 ± 11.3 mm^3/kJ, and 3-ms gaps had 15.2 ± 9.0 mm^3/kJ. The 200 W experiments clearly performed less efficiently than the 300 W ones, having average VE values of 8.9 ± 4.0 mm^3/kJ and 17.9 ± 5.8 mm^3/kJ, respectively.

The few experiments performed with a laser power of 100 W show DE values comparable to the higher power levels, an average of 0.648 +/- 0.287 mm/J, but much lower VE values, an average of 4.9 +/- 1.2 mm^3/kJ (Table 3).

The processing efficiencies of the continuous-mode experiments show that DE suffers greatly even compared to the lowest values produced by pulsed experiments (average DE for continuous-mode was 0.114 ± 0.013 mm/J, and the lowest pulsed-mode was 0.236 mm/J) whereas the VE values are comparable to their pulsed counterparts, with an average VE of 18.2 ± 6.837 mm^3/kJ (Table 4).

The experiments that were duplicated show that wide scatter is possible for all three samples (Table 5). In terms of relative deviations, the results suggest that values for DE can vary from 3.4% to 104.0% for olivine, 8.6% to 37.1% for pyroxene, and 12.3% for serpentine. The VE values vary from 1.0% up to 78.6% for olivine, 43.3% to 54.5% for pyroxene, and 23.0% for serpentine.

The shape, color, and width of the holes were different between samples, as well as different on each sample too (Fig. 11). The top two rows are olivine, the third row is pyroxene, and last row is serpentine. The olivine mostly has dark/metallic holes, with the exception of two of

Table 5
Average efficiencies and standard deviations for duplicate experiments. The letter c is for the continuous-mode experiment, which is 1 pulse 313 ms in length. VE stands for volume efficiency, DE for depth efficiency, and SD for standard deviation.

Material	Power (W)	Pulse width (ms)	Rep. rate (Hz)	Average VE (mm^3/kJ)	Std. Dev. VE (mm^3/kJ)	Average DE (mm/J)	Std. Dev. DE (mm/J)
Olivine	100	4	167	5.625	4.419	1.063	1.105
Olivine	200	2	333	9.327	0.408	0.745	0.136
Olivine	200	8	91	10.651	2.429	0.598	0.163
Olivine	300	8	111	25.243	0.246	0.441	0.015
Olivine	300	c	c	19.375	7.496	0.121	0.005
Pyroxene	300	4	200	31.081	16.934	0.320	0.119
Pyroxene	300	16	59	28.472	12.339	0.420	0.036
Serpentine	300	16	53	17.465	4.016	0.413	0.051

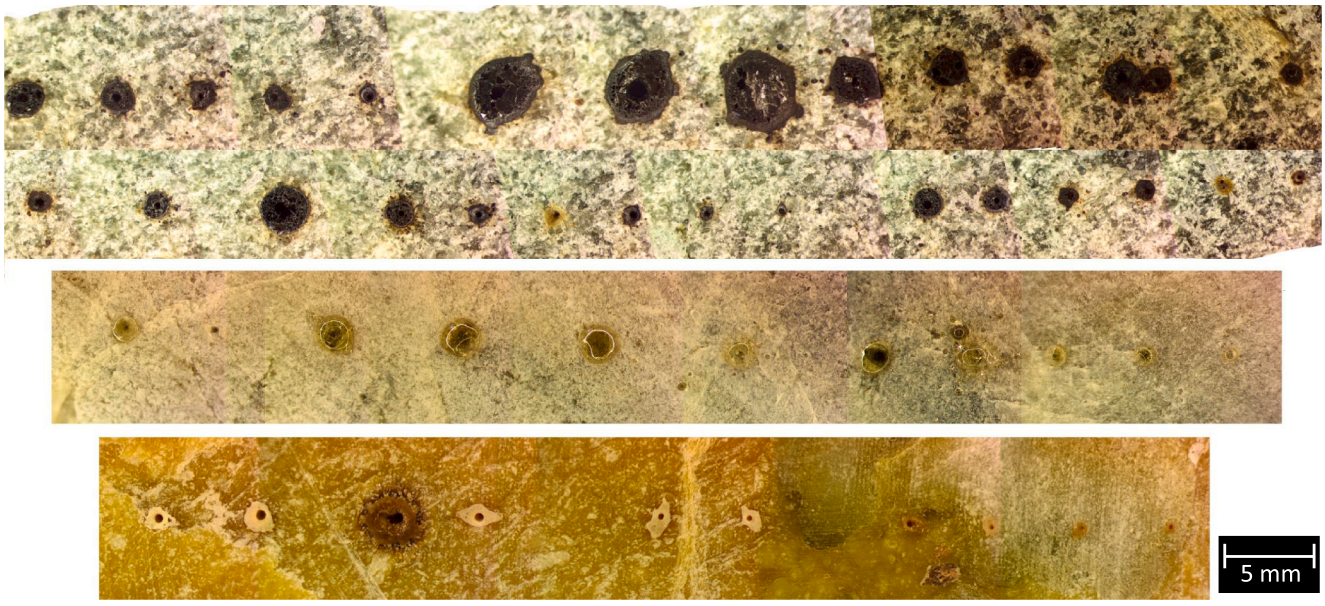

Fig. 11. View of holes on all three samples. The top panel is olivine, the middle panel is pyroxene, and bottom panel is serpentine. Individual images were taken of each hole under a microscope that were then stitched together. The images have the same size scale and can thus be directly compared to each other. Continuous-mode experiments are the largest of the series: middle center for olivine and 3rd from left on pyroxene and serpentine. Small holes on the far right were made by 100-W settings.

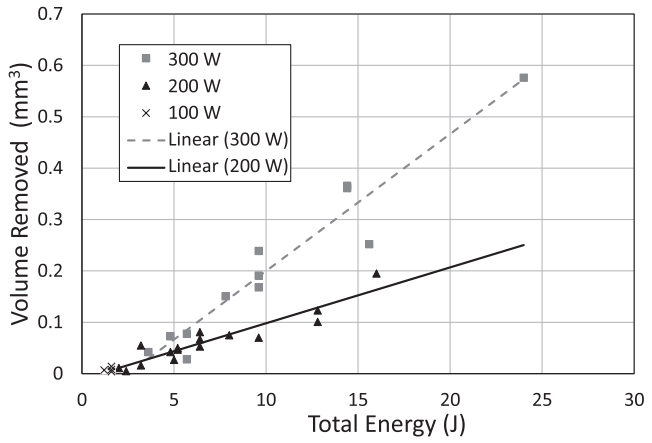

Fig. 12. Plot of volume removed against the total energy for the experiment for the olivine sample.

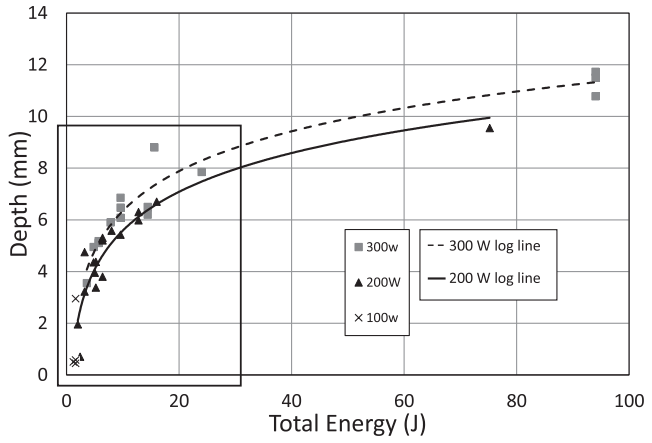

Fig. 13. Plot of the depth of the holes made in olivine versus how much total energy was used to make them. The box shows the region of experiments with pulsed settings, and the data points outside the box correspond to continuous-mode irradiation.

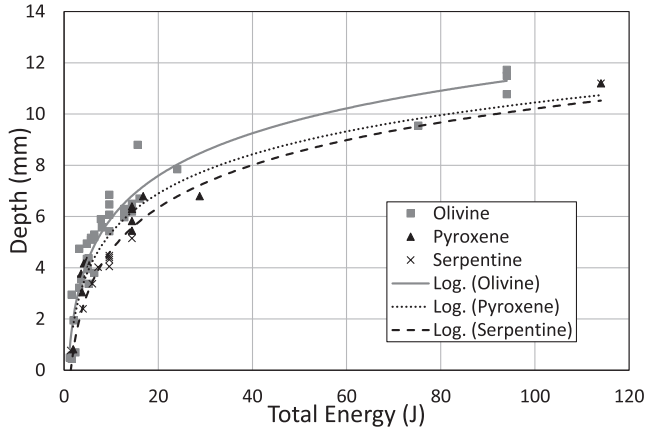

Fig. 14. Plot of depth of the holes made in all three samples versus how much total energy was used to make them. The depths for the pyroxene and serpentine were the same, so the data points overlap.

them, the hole second from the right on the bottom row, and sixth from the left on the bottom row. The pyroxene mostly has yellow holes, with the exception of the second from the left, which is white. Each of the non-white holes has a glassy coating. The serpentine holes vary the most, with white holes and brown holes over different regions of the material.

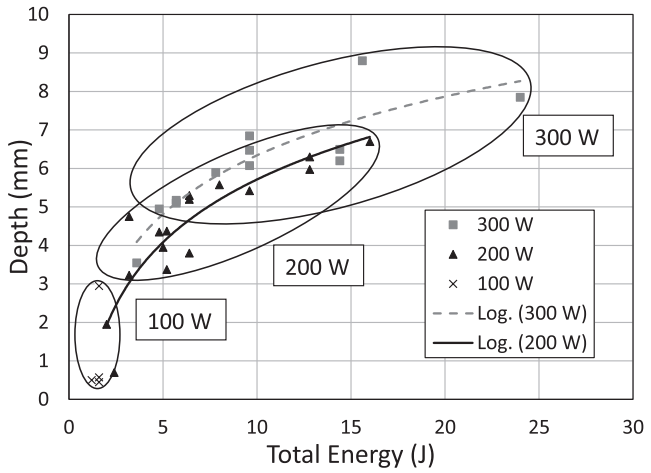

Fig. 15. Plot of the depth of the holes made in olivine versus how much total energy was used to make them. Here we only consider pulsed laser.

Comparing the wide range of settings used to make holes in the olivine sample, there appears to be a linear relationship between the total energy of the experiment and the volume of material removed from the hole (Fig. 12). The slope of the line increases relative to higher laser power, i.e., the higher the power, the steeper the slope. There is no 100-W trend line as there were only four experiments, and thus the trend cannot be accurately modelled. Although we note that they appear at the bottom left of the plot with some of the lowest volumes removed.

Another trend is a decreasing logarithmic relationship between the total energy and the depth of the hole (Fig. 13). The same logarithmic relationship between energy and depth holds true for the other three samples, where olivine appears to be be easiest to process, followed by pyroxene and then serpentine (Fig. 14). In addition, it is clear that higher laser power produces deeper holes (Fig. 15).

4. Discussion and additional analysis

In general, serpentine had smaller holes than olivine and pyroxene. The size difference could be due to the fundamental difference in crystal structure and chemical composition of the materials. Unlike olivine and pyroxene, serpentine contains water, which is located between layers of SiO_4 tetrahedra and AlO_6 octahedra. The energy entering the mineral might be absorbed by the water and dissipated from the hole area, if not simply expanding between the layers without melting or breaking. The distinct spattering behavior of serpentine may thus be due to its water content in combination with its layered structure, and in particular the dehydroxylation process at high temperatures.

The specific energy (reciprocal of VE) for slate and sandstone are in the range of 1 to 2 kJ/cm^3 at power densities of roughly 1 kW/cm^3 [16]. The minimum values we calculated for olivine, pyroxene, and serpentine were 36.5, 23.2, and 43.0 kJ/cm^3, respectively, but our power densities were on the order of 900 kW/cm^3. Slate and sandstone are "weaker" rocks, and would thus have lower specific energies overall. The specific energies for different rocks are within about one order of magnitude of each other, so there does not appear to be a radical difference between the energies required to process various stones. Another finding from [16] was that increasing the repetition rate reduced the specific energy. We cannot confirm this relationship, as only six of 13 instances showed such a trend. This could be due to the difference in power intensities and the corresponding difference in removal mechanisms (i.e. spallation vs spattering). We can also estimate the temperatures achieved in the experiment using the specific energy and specific heat capacities; the temperatures varied quite a lot, between 5 254 K and 141 414 K, but

averaged at 22 423 K.

Results from [32] showed mass removal rates near the "beginning" of their experiments of 2.1×10^{-7} kg/s, and near the "end" it was down to 2.5×10^{-8} kg/s. Their experiments ran for 10 min in continuous mode, and it is not clear exactly how they define the beginning of their experiments. We note that their model only considered sublimation, not spallation or melt ejection. The maximum removal rate in our experiments was 4.1×10^{-5} kg/s; the significant difference in magnitude suggests that a vast majority of material is ejected in the initial moments of laser beam irradiation.

The experiments by [32] were performed in a vacuum chamber, where atmospheric disturbances could not affect the processing. These disturbances could include melt pool pressure, turbulence, or eddy currents; lower ambient pressure could also allow vapour in the hole to escape easier, perhaps creating narrower holes. The spatter may behave differently, as it is unclear from the HSI whether the bubbles formed contained atmospheric gas or vapor from the processing.

The time required to ablate material has a considerable impact on mission design, primarily regarding whether or not a spacecraft is required to land on the surface or if it can stay in orbit near the asteroid. The ability to maintain the location of the focal point of the laser on the asteroid surface is difficult from orbit, and would require highly precise control equipment, whereas a lander would have little issue with spot control. Our results suggest that, if the aim is to redirect an asteroid by removing surface material to produce a momentum exchange, maintaining precise control is not necessary. The beam spot can wander around on the surface, within limits, spallating and melting new locations, rather than being focused on one spot to operate in the vapor ablation state.

The decreasing logarithmic relationship between depth and total energy might be due to the fact that the laser beam de-focuses with distance from the focal point. The continuous-mode experiments (the longest/most energetic) produced the deepest holes, nearly penetrating the olivine sample, but still did not go deeper than 10–12 mm. This relationship only holds for the range of energies used in this experiment; longer exposure will eventually reach a maximum depth, when the laser beam de-focuses to the point where it can no longer process material. Using the spot size of 0.1 mm and beam quality of 8 mm mrad, we can see that after 1 cm, the beam is roughly 0.8 mm, eight times wider than in focus.

The experiment setup was not designed to study any gas or vapor. Ablated vapor can block some of the incident laser irradiation, and it can occur within the first nanosecond of exposure. It must be noted that the presence of the vapor and the spattering ejecta must have blocked some of the laser beam, which could have affected the shape of the hole and the total amount of material removed.

The results showed relatively large scatter (~20%) although the measurements were relatively accurate (<2% error). This implies that the differences in the results are most likely due to the micro-scale material properties and/or pulse parameter settings. This is further demonstrated when considering the results obtained by multiple experiments at the same pulse parameter settings. The wide range of variability of VE and DE in olivine are most likely due to the local concentrations of forsterite and fayelite. The pyroxene and serpentine also showed relatively large variations in efficiencies, which can more readily be explained by larger-scale composition differences.

While the laser was able to process all three rocks in a similar fashion, we can only speculate how it will affect other materials. We know asteroids are not entirely homogeneous, and may contain pockets of metals, hydrocarbons, or other volatiles, which may react differently, depending on their absorption at the laser frequency.

There is also clearly a presence of re-deposited material on the surface. The build-up could be due to the shielding gas being angled slightly towards the surface, though the HSI does not show a uniform movement of all particles. Alternatives include electrostatic forces and local drag due to the expansion of the local ambient atmosphere.

5. Conclusions

The cross-disciplinary approach utilized in the present research project provided several insights into how lasers can efficiently be used to process asteroid material.

First, regardless of the material, the laser was able to produce similar melting and ejection behavior for all three samples. A 1070-nm laser is demonstrated to reliably and robustly process olivine, pyroxene, and serpentine, even at 100 W, the lowest power used in the present research project. The relatively small energy consumption and high processing efficiency therefore suggest that laser payloads are suitable for small satellites with limited power budgets.

Second, spatter produced during the first pulse is significantly smaller and faster than spatter produced later in the same experiment in both pyroxene and olivine. Serpentine did not have a rapid-outburst phase, it immediately began to melt and behaved like a mid-depth process.

Third, there is clear evidence of forces that keep more material from being ejected. These can include surface tension, wetting forces, and atmospheric pressure.

Fourth, our measurements suggest there is a trade-off with pulse length between depth and volume removal efficiencies. Short pulses make deeper holes, but longer pulses are preferred for removing the most amount of volume.

Fifth, the depth efficiency seems to be inversely related to pulse repetition rate, but volume efficiency is directly related. The continuous-mode experiments had the poorest depth efficiency.

The HSI and XMT data as well as microscope imaging of the holes are available upon request.

CRediT authorship contribution statement

Niklas Anthony: Conceptualization, Methodology, Formal analysis, Investigation, Writing - original draft, Visualization, Project administration. **Jan Frostevarg:** Conceptualization, Methodology, Resources, Writing - review & editing, Supervision, Funding acquisition. **Heikki Suhonen:** Software, Investigation, Resources, Writing - review & editing, Visualization. **Christina Wanhainen:** Conceptualization, Resources, Writing - review & editing. **Antti Penttilä:** Investigation, Writing - review & editing, Visualization. **Mikael Granvik:** Conceptualization, Methodology, Investigation, Resources, Writing - review & editing, Visualization.

Declaration of Competing Interest

The authors declare that they have no known competing financial interests or personal relationships that could have appeared to influence the work reported in this paper.

Appendix A

Figs. A.1–A.7.

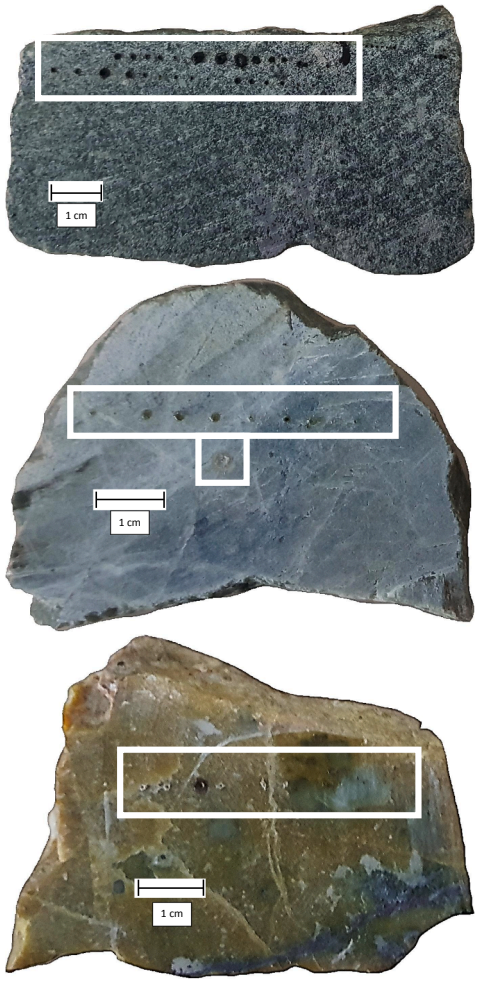

Fig. A.1. Images of the samples showing overall macroscopic characteristics; from top to bottom, they are: olivine, pyroxene, and serpentine. The white boxes show where the experiments were performed.

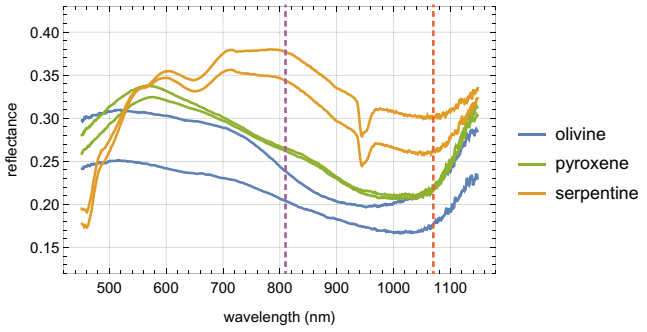

Fig. A.2. Reflectance spectra of the samples. The spectra was measured in two separate spots, both presenting the typical phase of the sample, for all the three samples. The wavelength of the laser at 1070 nm is indicated with a red, dashing line in the figure, and the wavelength of the illumination for the high-speed camera at 810 nm with a violet, dashed line.

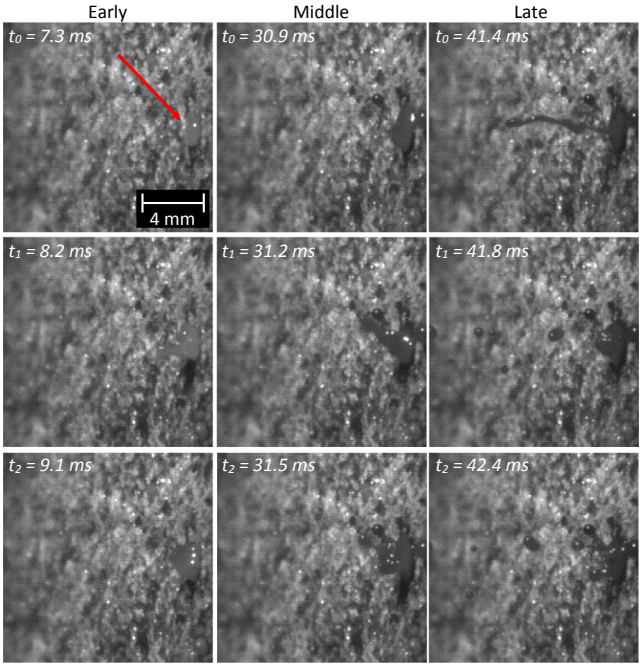

Fig. A.3. High-speed footage of olivine experiment over time. The power setting was 300 W, pulse length 8 ms, and pulse gap 3 ms.

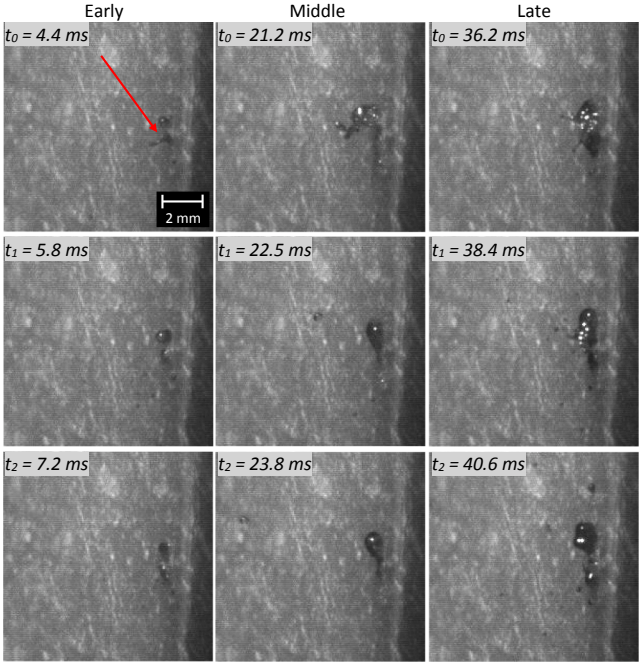

Fig. A.4. High-speed footage of serpentine experiment over time. The power setting was 300 W, pulse length 8 ms, and pulse gap 3 ms.

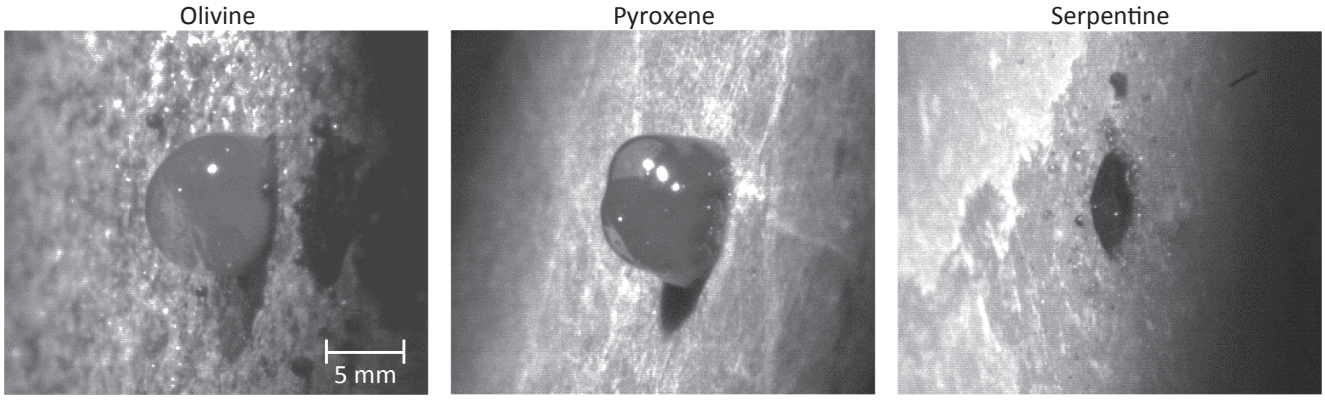

Fig. A.5. Images showing the formation of translucent bubbles briefly after laser irradiation has ended.

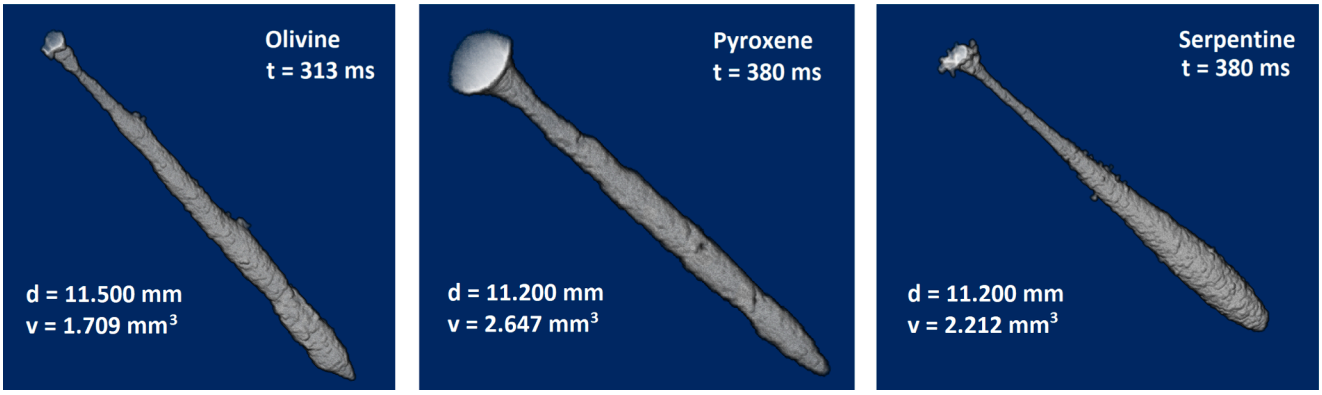

Fig. A.6. XMT images of the continuous-mode experiments at 300 W. Shown are the d for depth and v for volume as well as duration of each experiment.

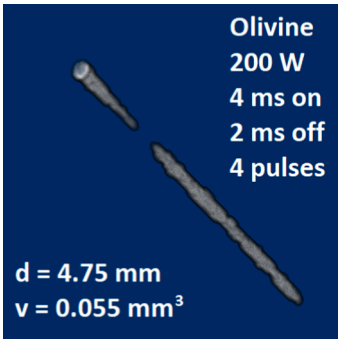

Fig. A.7. XMT images of a hole in olivine exhibiting a bottle-neck. The hole corresponds to a laser power of 200 W with the irradiation being on for 4 ms and off for 2 ms.

Appendix B. Supplementary material

Supplementary data associated with this article can be found, in the online version, at https://doi.org/10.1016/j.optlastec.2020.106724.

References

[1] D.G. Andrews, K. Bonner, A. Butterworth, H. Calvert, B. Dagang, K. Dimond, L. Eckenroth, J. Erickson, B. Gilbertson, N. Gompertz, O. Igbinosun, T. Ip, B. Khan, S. Marquez, N. Neilson, C. Parker, E. Ransom, B. Reeve, T. Robinson, M. Rogers, P. Schuh, C. Tom, S. Wall, N. Watanabe, C. Yoo, Defining a successful commercial asteroid mining program,", Acta Astronaut. 108 (2015) 106–118, https://doi.org/10.1016/j.actaastro.2014.10.034.
[2] M. Gaffey, T. Mccord, Mining outer space, Technol. Rev. 79 (7) (1977) 51–59.
[3] B. O'Leary, Mining the apollo and amor asteroids, Science 197 (4301) (1977) 363–366, https://doi.org/10.1126/science.197.4301.363-a, issn: 0036-8075.
[4] C.B. Dreyer, J. Sercel, L. Gertsch, A. Lampe, T.J. Canney, A. Abbud-Madrid, Optical mining subscale testing, Earth Space (2016, 2016,) 493–506, https://doi.org/10.1061/9780784479971.047.
[5] Pekka Janhunen, Shielded Dumbbell L5 Settlement, NSS Space Settlement Journal, vol. 4, pp. 1–11, 2020. Available: https://space.nss.org/wp-content/uploads/NSS-JOURNAL-Shielded-Dumbbell-L5-Settlement.pdf.
[6] T.H. Prettyman, N. Yamashita, M.J. Toplis, H.Y. McSween, N. Schörghofer, S. Marchi, W.C. Feldman, J. Castillo-Rogez, O. Forni, D.J. Lawrence, E. Ammannito, B.L. Ehlmann, H.G. Sizemore, S.P. Joy, C.A. Polanskey, M. D. Rayman, C.A. Raymond, C.T. Russell, Extensive water ice within Ceres' aqueously altered regolith: Evidence from nuclear spec-troscopy, Science 355 (6320) (Jan. 2017) 55–59, https://doi.org/10.1126/science.aah6765.
[7] K. Zacny, P. Chu, G. Paulsen, M. Hedlund, B. Mellerow-icz, Asteroids: Anchoring and Sample Acquisition Approaches in Support of Science, Exploration, and In situ Resource Utilization, in: V. Badescu (ed.), Asteroids: Prospective Energy and Material Resources, 2013, pp. 287–343. doi: 10.1007/978-3-642-39244-3_12.
[8] J.P. Singh, S.N. Thakur, Laser-induced Breakdown Spectroscopy, Elsevier Science, 2007, https://doi.org/10.1016/B978-0-444-51734-0.X5001-7.
[9] T.H. Maiman, Stimulated optical radiation in ruby, Nature 187 (4736) (1960) 493–494, https://doi.org/10.1038/187493a0.
[10] I.F. Larsson, Method and apparatus for drilling holes by means of a focused laser beam, no. USA, Patent Nr. US3410979A, 1964, 1964.
[11] M. von Allmen, Laser drilling velocity in metals, J. Appl. Phys. 47 (12) (1976) 5460–5463, https://doi.org/10.1063/1.322578.
[12] D.K.Y. Low, L. Li, P.J. Byrd, The effects of process parameters on spatter deposition in laser percussion drilling, Opt. Laser Technol. 32 (5) (2000) 347–354, https://doi.org/10.1016/S0030-3992(00)00079-7.
[13] J. Pocorni, J. Powell, J. Frostevarg, A.F.H. Kaplan, Investigation of the piercing process in laser cutting of stainless steel, J. Laser Appl. 29 (2) (2017) 022201-1–022201-8, https://doi.org/10.2351/1.4983260.
[14] M. Schneider, L. Berthe, R. Fabbro, M. Muller, M. Nivard, Gas investigation for laser drilling, J. Laser Appl. 19 (3) (2007) 165–169, https://doi.org/10.2351/1.2567844.
[15] C. Lehane, H. Kwok, Enhanced drilling using a dual-pulse nd:yag laser, Appl. Phys. A 73 (2001) 45–48, https://doi.org/10.1007/s003390100819.
[16] Z. Xu, C.B. Reed, G. Konercki, R.A. Parker, B.C. Gahan, S. Batarseh, R.M. Graves, H. Figueroa, N. Skinner, Specific energy for pulsed laser rock drilling, J. Laser Appl. 15 (1) (2003) 25–30, https://doi.org/10.2351/1.1536641.
[17] A. Riveiro, A. Mejías, R. Soto, F. Quintero, J. [Val], M. Boutinguiza, F. Lusquiños, J. Pardo, J. Pou, CO2 laser cutting of natural granite, Opt. Laser Technol. vol. 76, pp.

19–28, 2016. doi: https://doi. org/ 10.1016/j.optlastec.2015.07.018, issn: 0030-3992.
[18] M. Boutinguiza, J. Pou, F. Lusquiños, F. Quintero, R. Soto, M. Pérez-Amor, K. Watkins, W. Steen, CO2 laser cutting of slate, Opt. Lasers Eng. 37 (1) (2002) 15–25, https://doi.org/10.1016/S0143-8166(01)00142-7, issn: 0143-8166.
[19] O. Kotova, N. Leonenko, Physics and chemistry of minerals under laser processing, in: Materials Science and Engineering Conference Series, ser. Materials Science and Engineering Conference Series, vol. 123, Apr. 2016, p. 012 016. doi: 10.1088/1757-899X/123/1/012016.
[20] N. Leonenko, E. Vanina, G. Kapustina, E. Veselova, Study of nonlinear effect about laser-induced processes of nanodis-persed gold in mineral association, in: Material Researches and Energy Engineering, ser. Advanced Materials Research, vol. 772, Trans Tech Publications Ltd, Nov. 2013, pp. 355–358. doi: 10.4028/www.scientific.net/AMR. 772.355.
[21] M. Norman, P. Robinson, D. Clark, MAJOR- AND TRACE-ELEMENT ANALYSIS OF SULFIDE ORES BY LASER-ABLATION ICPfffdfffdfffdMS, SOLUTION ICPfffdfffdfffdMS, AND XRF: NEW DATA ON INTERNATIONAL REFERENCE MATERIALS, Can. Mineral. 41 (2) (2003) 293–305, https://doi.org/10.2113/gscanmin.41.2.293, issn: 0008-4476.
[22] R.Z. Sagdeev, A.V. Zakharov, Brief history of the Phobos mission, Nature 341 (6243) (Oct. 1989) 581–585, https://doi.org/10.1038/341581a0.
[23] R.C. Wiens, S. Maurice, B. Barraclough, M. Saccoccio, W.C. Barkley, J.F. Bell, S. Bender, J. Bernardin, D. Blaney, J. Blank, M. Bouyé, N. Bridges, N. Bultman, P. Caïs, R.C. Clan-ton, B. Clark, S. Clegg, A. Cousin, D. Cremers, A. Cros, L. DeFlores, D. Delapp, R. Dingler, C. D'Uston, M. Darby Dyar, T. Elliott, D. Enemark, C. Fabre, M. Flores, O. Forni, O. Gas-nault, T. Hale, C. Hays, K. Herkenhoff, E. Kan, L. Kirkland, D. Kouach, D. Landis, Y. Langevin, N. Lanza, F. LaRocca, J. Lasue, J. Latino, D. Limonadi, C. Lindensmith, C. Little, N. Mangold, G. Manhes, P. Mauchien, C. McKay, E. Miller, J. Mooney, R.V. Morris, L. Morrison, T. Nelson, H. Newsom, A. Ollila, M. Ott, L. Pares, R. Perez, F. Poitrasson, C. Provost, J.W. Reiter, T. Roberts, F. Romero, V. Sautter, S. Salazar, J.J. Simmonds, R. Stiglich, S. Storms, N. Striebig, J.-J. Tho-caven, T. Trujillo, M. Ulibarri, D. Vaniman, N. Warner, R. Waterbury, R. Whitaker, J. Witt, B. Wong-Swanson, The ChemCam Instrument Suite on the Mars Science Laboratory (MSL) Rover: Body Unit and Combined System Tests, Space Science Reviews, vol. 170, no. 1-4, pp. 167-227, Sep. 2012. doi: https://doi.org/10.1007/s11214-012-9902-4.
[24] P.S. Moura, B. Serpa, B. Assis, Y. Moura, V.P. Alves, K.A. Schenguer, B.L. Tumelero, A. Luz, L.G.C. Novaes, A.T. Cabral, D.V. Rotter, N. Rossini, P.M.R. Santos, T.K. Bretzke, M. de Souza, K. Morais, D. Champoski, D. Vieira, G. Spricigo, E.D. Carli, S.L.S. Taglialenha, G.B. Hughes, A CubeSat mission for space-environment demonstration of Remote Laser-Evaporative Molecular Absorption (R-LEMA) spectroscopy sensor system concept, in: T.S. Pagano, C.D. Norton (Eds.), CubeSats and NanoSats for Remote Sensing II, International Society for Optics and Photonics, vol. 10769, SPIE, 2018, pp. 164–173. doi: 10.1117/12.2320863.
[25] R.P. Binzel, F.E. DeMeo, E.V. Turtelboom, S.J. Bus, A. Tokunaga, T.H. Burbine, C. Lantz, D. Polishook, B. Carry, A. Morbidelli, M. Birlan, P. Vernazza, B.J. Burt, N. Moskovitz, S.M. Slivan, C.A. Thomas, A.S. Rivkin, M.D. Hicks, T. Dunn, V. Reddy, J.A. Sanchez, M. Granvik, T. Ko-hout, Compositional distributions and evolutionary processes for the near-Earth object population: Results from the MIT-Hawaii Near-Earth Object Spectroscopic Survey (MITHNEOS), Icarus 324 (2019) 41–76, https://doi.org/10.1016/j.icarus.2018.12.035.
[26] V. Reddy, T.L. Dunn, C.A. Thomas, N.A. Moskovitz, T.H. Burbine, Mineralogy and Surface Composition of Asteroids, in: P. Michel, F.E. DeMeo, W.F. Bottke (Eds.), Asteroids IV, 2015, pp. 43–63. doi: 10.2458/azu_uapress_9780816532131-ch003.
[27] A.E. Rubin, Mineralogy of meteorite groups, Meteoritics Planet. Sci. 32 (1997) 231–247, https://doi.org/10.1111/j.1945-5100.1997.tb01262.x.
[28] F. Deer W.A., R.A. Howie, J. Zussman, An introduction to the rock-forming minerals. Mineral. Soc. Great Britain and Ireland, Jan. 2013, isbn: 9780903056274. doi: 10.1180/DHZ.
[29] N.L. Bowen, J.F. Schairer, The system MgO-FeO-SiO2, Am. J. Sci. 29 (5) (1935) 151–217, https://doi.org/10.2475/ajs.s5-29.170.151.
[30] G.C.C. Costa, N.S. Jacobson, J. Fegley Bruce, Vaporization and thermodynamics of forsterite-rich olivine and some implications for silicate atmospheres of hot rocky exoplanets, vol. 289, pp. 42–55, Jun. 2017. doi: 10.1016/j.icarus.2017.02.006.
[31] H.J. Melosh, I.V. Nemchinov, Y.I. Zetzer, Non-nuclear strategies for deflecting comets and asteroids, in: Hazards Due to Comets and Asteroids, Jan. 1994, pp. 1111–1132.
[32] A. Gibbings, M. Vasile, I. Watson, J.-M. Hopkins, D. Burns, Experimental analysis of laser ablated plumes for asteroid deflection and exploitation, Acta Astronautica, vol. 90, no. 1, pp. 85–97, 2013, NEO Planetary Defense: From Threat to Action - Selected Papers from the 2011 IAA Planetary Defense Conference, issn: 0094–5765. doi: https://doi.org/10. 1016/j.actaastro.2012.07.008.
[33] J. Sloane, Laser ablation propulsion of asteroids with a sub-nanosecond pulsed laser, PhD thesis, University of Maryland, College Park, 2019.
[34] C.T. Rueden, J. Schindelin, M.C. Hiner, B.E. DeZonia, A.E. Walter, et al., Image J2: ImageJ for the next generation of scientific image data, BMC Bioinformatics 18 (2017) 529, https://doi.org/10.1186/s12859-017-1934-z.
[35] J. Schindelin, I. Arganda-Carreras, E. Frise, V. Kaynig, M. Longair, T. Pietzsch, S. Preibisch, C. Rueden, S. Saalfeld, B. Schmid, J.-Y. Tinevez, D.J. White, V. Hartenstein, K. Eliceiri, P. Tomancak, A. Cardona, Fiji: An open-source platform for biological-image analysis, Nat. Methods 9 (7) (2012) 676–682, https://doi.org/10.1038/nmeth.2019.